Single-molecule optical absorption imaging by nanomechanical photothermal sensing

Miao-Hsuan Chien[a], Mario Brameshuber[b], Benedikt K. Rossboth[b], Gerhard J. Schütz[b], and Silvan Schmid[a,1]

[a]Institute of Sensor and Actuator Systems, TU Wien, 1040 Vienna, Austria; and [b]Institute of Applied Physics, TU Wien, 1040 Vienna, Austria

Edited by W. E. Moerner, Stanford University, Stanford, CA, and approved August 28, 2018 (received for review March 12, 2018)

Absorption microscopy is a promising alternative to fluorescence microscopy for single-molecule imaging. So far, molecular absorption has been probed optically via the attenuation of a probing laser or via photothermal effects. The sensitivity of optical probing is not only restricted by background scattering but it is fundamentally limited by laser shot noise, which minimizes the achievable single-molecule signal-to-noise ratio. Here, we present nanomechanical photothermal microscopy, which overcomes the scattering and shot-noise limit by detecting the photothermal heating of the sample directly with a temperature-sensitive substrate. We use nanomechanical silicon nitride drums, whose resonant frequency detunes with local heating. Individual Au nanoparticles with diameters from 10 to 200 nm and single molecules (Atto 633) are scanned with a heating laser with a peak irradiance of 354 ± 45 μW/μm^2 using 50× long-working-distance objective. With a stress-optimized drum we reach a sensitivity of 16 fW/Hz$^{1/2}$ at room temperature, resulting in a single-molecule signal-to-noise ratio of >70. The high sensitivity combined with the inherent wavelength independence of the nanomechanical sensor presents a competitive alternative to established tools for the analysis and localization of nonfluorescent single molecules and nanoparticles.

photothermal microscopy | single-molecule imaging | nanomechanical sensing | nanoelectromechanical systems | nanoparticle absorption analysis

Optical single-molecule detection techniques have become indispensable tools in a great variety of fields of the scientific community over the past decades. Not only does the high sensitivity enable trace analysis of minute samples, but the analysis of single molecules also provides insight into the individual properties, which may differ from the statistical average behavior of bulk samples. Optical fluorescent single-molecule detection has become an enabling technology underlying applications such as single-molecule tracking or superresolution microscopy (1, 2). However, emission states of fluorophores can be easily quenched or destroyed by photochemical interactions under ambient conditions, resulting in photobleaching or blinking. Furthermore, fluorescent labeling has shown to possibly weaken the intermolecular electrostatic interactions and therefore change the dynamics of the system under test (3). Effort has thus been made over the past decades in the development of various label-free imaging techniques based on the measurements of optical scattering, extinction, and absorption (4, 5). Label-free optical single-molecule detection is of fundamental interest among a great variety of fields, ranging from tracking and quantification of components in cell biology (6, 7) such as viruses, proteins, and antibodies, applications in high-accuracy medical diagnostics (8–12), to environmental monitoring (13, 14). Moreover, typical limitations given by photochemical instabilities of fluorescent markers, such as photobleaching, can be overcome.

In contrast to optical scattering cross-sections, which scale quadratically with the volume of a scattering object, optical absorption cross-sections scale linearly with the volume of the absorber. Hence, absorption-based techniques are highly effective for the detection and imaging of samples, such as nanoparticles, smaller than ∼100 nm (15). Since the first direct cryogenic single-molecule absorption measurement was demonstrated with laser frequency modulation techniques by Moerner and Kador (16), many absorption-based techniques have been developed and successfully implemented for imaging of nanoobjects at room temperature. Such absorption-based techniques include: photothermal microscopy (17–25), scanning interferometric imaging (26, 27), spatial modulation microscopy (28), direct absorption (29, 30), transient absorption microscopy (31), ground-state depletion microscopy (32), and whispering-gallery–mode resonator sensing (33).

Among these state-of-the-art techniques, single-molecule sensitivity has been achieved by direct optical absorption microscopy (29, 30) and ground-state depletion microscopy (32). However, the detection of the minute relative light attenuation on the order of 10^{-7}–10^{-6}, caused by the photon absorption of a single molecule, is challenging. The sensitivity is limited not only by scattering due to variations of refractive index in the sample, but fundamentally by shot noise of the probing laser, resulting in shot-noise-limited sensitivities on the order of a few picowatts per square root hertz (30, 32).

Alternatively, imaging techniques based on the photothermal heating of a sample, such as photothermal contrast microscopy (17, 19) and photothermal heterodyne imaging (8, 20), have been demonstrated. Here, the photothermal heating is detected optically via the thermal change in refractive index of the medium in the vicinity of the light-absorbing sample. Using a medium with a highly temperature-sensitive refractive index is a way to enhance the sensitivity. Single-molecule imaging has been

Significance

Absorption microscopy is a promising technique that can detect single nonfluorescent molecules. However, fundamental limitations of existing optical absorption methods result in noisy detection signals for single molecules, which has hindered many anticipated applications. A promising method is to optically measure the photothermal heating of single molecules. In this paper, we present a photothermal microscopy technique where we detect the photothermal heating of single molecules mechanically with a temperature-sensitive nanomechanical drum. With our method, we achieve an unprecedented optical absorption sensitivity, enabling the detection of single molecules with large signal-to-noise ratios. This enables interesting applications such as the accurate localization of naturally occurring marker molecules or the identification of single molecules by measuring their absorption spectrum.

Author contributions: M.-H.C., G.J.S., and S.S. designed research; M.-H.C., M.B., and B.K.R. performed research; M.B., B.K.R., and G.J.S. contributed new reagents/analytic tools; M.-H.C., M.B., B.K.R., G.J.S., and S.S. analyzed data; and M.-H.C., M.B., G.J.S., and S.S. wrote the paper.

The authors declare no conflict of interest.

This article is a PNAS Direct Submission.

See Commentary on page 11115.

[1]To whom correspondence should be addressed. Email: silvan.schmid@tuwien.ac.at.

This article contains supporting information online at www.pnas.org/lookup/suppl/doi:10.1073/pnas.1804174115/-/DCSupplemental.

Published online September 25, 2018.

achieved by using glycerol as medium, resulting in a sensitivity of a few nanowatts per square root hertz (18). Compared with glycerol, a 10-fold increase in sensitivity has been achieved with thermotropic liquid crystals (24), and a hundreds-fold increase has been achieved with near-critical Xe (23). The outstanding sensitivity of a few tens of picowatts per square root hertz of the latter method however requires the control of temperature and pressure to be near the critical point of Xe. It has further been shown that the photothermal heating of a sample can efficiently be detected with an optical whispering-gallery mode resonator, acting as an ultrasensitive thermometer (33). Along the same line, photothermal detection with thermally sensitive nanooptomechanical systems had been proposed (18) to amplify the photothermal signal. Indeed, it has been shown that the absorption of single gold nanostructures (34) and polymer nanoparticles (35) can directly be detected via the photothermally induced frequency detuning of nanomechanical string resonators. In essence, the sample substrate acts as the thermometer, which detects the local photothermal heating of sample such as nanoparticles or molecules.

Here, we introduce nanomechanical photothermal microscopy, based on drum resonators, as an optical platform for single-nanoparticle and single-molecule imaging and analysis. Our work is based on silicon nitride nanodrums with a typical thickness of 50 nm, which are commonly used as windows for transmission electron microscopy or X-ray diffraction analysis due to their low and featureless background absorption for electrons and photons in the visible- to near-infrared regime. In contrast to previously used silicon nitride string resonators, silicon nitride drums are robust, which readily allow liquid handling and sampling, such as drop-casting and spin-coating, etc. Furthermore, such nanomechanical silicon nitride drums are available commercially (Norcada, Inc.). Compared with strings, drum resonators have a significantly lower frequency responsivity to photothermal heating. We overcome this limitation by an oxygen-plasma–induced tuning of the intrinsic tensile stress of the silicon nitride drums, ultimately resulting in frequency responsivities enabling single-molecule detection with large signal-to-noise ratios.

The working principle of our method is depicted in Fig. 1*A*. When the scanning probe laser hits a sample, the optical absorption of the sample causes local heating and a heat flux into the drum resonator. The corresponding thermal expansion reduces the stress of the drum, which causes a detectable detuning in the mechanical resonance frequency. The scanning of the drum was done by a commercial laser-Doppler vibrometer (LDV) with a 633-nm readout laser and a long-working-distance 50× objective. In contrast to most single-molecule microscopy techniques, objectives with high numerical aperture or oil immersion is not a requirement in the present setup. The LDV laser functions simultaneously as pump and probe laser for the excitation of samples and the real-time readout of the drum vibration, respectively. This bypasses the complexity of multibeam optical alignments.

The resonance frequency of the drum is tracked with a phase-locked loop (PLL). Therefore, the analog signal from LDV is fed into a lock-in amplifier with integrated PLL functionality (HF2LI from Zurich Instruments). The drum is driven with a piezoelectric actuator that is connected to the lock-in amplifier output.

To reduce heat transfer from the drum to the surrounding gas, which would limit the photothermal heating and hence the sensitivity, all measurements are performed in vacuum below 10^{-4} mbar. At this pressure the thermal conductivity of air becomes insignificant. For practical reasons it is important to mention that the thermal conductivity of air already drops by more than 90% at a pressure of 10^{-3} mbar (36), which can readily be reached with, e.g., a rotary vane pump.

Imaging of Single 10-nm Au Nanoparticles

First, 10-nm gold nanoparticles (AuNPs) were imaged using an irradiance I of 354 ± 45 μW/μm^2 on a silicon nitride drum with tensile stress of ∼30 MPa. The mechanical resonance frequency of the silicon nitride drum was tracked with the PLL during scanning with constant integration time for each pixel, as shown in Fig. 1*B*. The scanning area is confined to a centered region with a diameter of ∼160 μm, to achieve a consistently high responsivity (*SI Appendix*, Fig. S2). A baseline correction, accounting for the existing lateral responsivity variation of the drum, is made for each line scan based on a one-dimensional median filter (red line in Fig. 1*B*). Then, the average drum-frequency shift (Δf) is calculated for each scan point, which is shown in Fig. 1*C*. The integration time for each scan point is ensured to be larger than the thermal relaxation time constant of ∼200 ms for the drum (*SI Appendix*, Fig. S3). From the individual 1D line scans, the 2D images are stitched together, as shown in

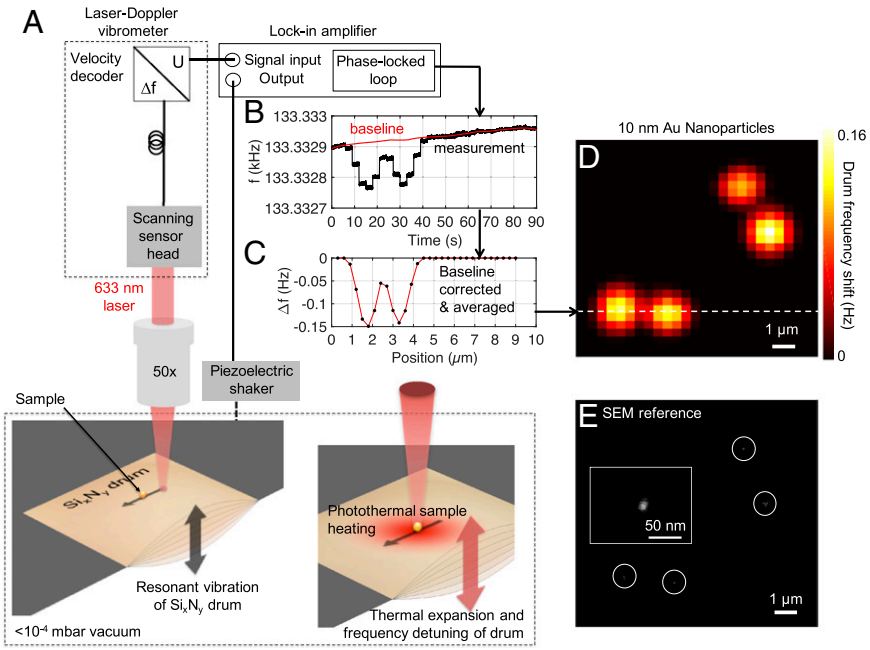

Fig. 1. (*A*) Schematic description of working principle and detection scheme. (*B*) PLL tracking of drum resonance frequency [fundamental (1,1) mode] for a line scan over two 10-nm Au particles with the 633-nm scanning laser with a power of 381 μW. The particles are measured on a silicon nitride drum with 30 MPa of tensile stress. (*C*) Frequency shift of the line scan after baseline correction and averaging over the integration time for each point. (*D*) Corresponding 2D scan of 10-nm gold NPs. (*E*) Reference SEM image of AuNPs with a higher magnification image in the inset.

Fig. 1*D*. A corresponding scanning electron microscopy (SEM) image of the same AuNPs is shown in Fig. 1*E*. The position of NPs in our scan overlaps perfectly with the corresponding SEM image.

Due to the dielectric nature of silicon nitride, the SEM imaging of the AuNPs on the drum was limited by the charging effect. In contrast, the thermal insulation of the dielectric drum is the basis of our high responsivity, which results in significantly enhanced imaging contrast, as shown in Fig. 1 *D* and *E*. Hence, nanomechanical photothermal microscopy provides an option for the imaging and analysis of NPs on poor- or nonconducting substrates, which could be challenging for SEM. More scans with corresponding SEM images of AuNPs with different diameter ranging from 30 to 200 nm are provided in *SI Appendix*, Fig. S4.

Analysis of AuNPs Absorption Cross-Section

Optical probing of plasmonic nanostructures typically yields the sample extinction, which is the sum of scattering and absorption. To show that nanomechanical photothermal microscopy uniquely allows for a pure absorption sample analysis, we studied single AuNPs with varying diameters, as shown in Fig. 2*A*. The average relative frequency shifts ($\delta f = \Delta f / f_0$) for the individual particles as a function of peak irradiance are plotted in Fig. 2*B*. From the relative frequency shifts, assuming 100% thermalization yield, the absorbed power P_{abs} can be calculated from

$$P_{abs} = \delta f / R, \qquad [1]$$

with R being the relative responsivity of the drum, which was measured each time before sampling (*SI Appendix*, Fig. S1). As expected, the measured relative frequency shifts for AuNPs of a specific dimension scale linearly with the used irradiance I of the laser beam. The absorption cross-section σ_{abs} can then be calculated by

$$\sigma_{abs} = P_{abs} / I, \qquad [2]$$

which is represented by the linear fits in Fig. 2*B*. In Fig. 2*C*, the extracted average σ_{abs} are plotted as a function of particle size. It shows that the σ_{abs} values follow the absorption model of the Mie theory with high accuracy (4), compared with the steeper slope expected for pure scattering, The advantage of detecting absorption instead of scattering becomes obvious from Fig. 2*C*, with the corresponding scattering cross-section decaying significantly faster for AuNPs with dimensions below 200 nm.

As shown in Fig. 2*C* (*Inset*), the current laser wavelength of 633 nm does not match the maximal absorption peak of small AuNPs. Switching to a laser with a wavelength closer to 500 nm, for example, would significantly improve the absorption signal of sub-10-nm AuNPs in particular. But even with the nonoptimal heating laser wavelength, we have shown the capability for a quantitative absorption analysis and imaging of plasmonic samples.

Effect of Tensile Stress on Responsivity

The relative responsivity of a rectangular nanomechanical drum can be described to a good approximation by (37)

$$R \approx \frac{\alpha E}{8\pi\kappa h\sigma}\left(\frac{2-\upsilon}{1-\upsilon} - 0.642\right), \qquad [3]$$

which is a first-order Taylor series approximation of the responsivity of a circular drum. The parameters are the thermal expansion coefficient $\alpha = 2.2\times10^{-6}$ K^{-1}, Young's modulus $E = 250$ GPa, thermal conductivity $\kappa = 3$ W/(m·K), Poisson's ratio $\upsilon = 0.23$, drum thickness $h = 50$ nm, and tensile stress σ. Obviously, the frequency response for a unit-absorbed power of a drum resonator can be enhanced by reducing the tensile stress σ. The relationship between tensile stress in the silicon nitride drum and its responsivity are thus investigated both experimentally and theoretically.

To analyze the effects of tensile stress and optimize the responsivity systematically, we used silicon nitride drums with an intrinsic tensile stress of 1 GPa, 250 MPa, and 30 MPa. A drum with 30 MPa was further treated with 50-W oxygen plasma to reduce the tensile stress (38). The oxygen plasma forms a thin silicon oxynitride layer with a compressive stress on the drum surface. In this way, the tensile stress was further reduced to 6, 1.2, and 0.8 MPa, respectively. In Fig. 3*A*, the experimentally obtained responsivities, based on the specific absorption cross-sections of the measured AuNPs, for all drums with varying stress are plotted and compared with the theoretical model (Eq. **3**). The measured responsivities follow the model with high accuracy. Only for the lowest tensile stress values, the model **3** based on the first-order Taylor series approximation (blue dashed line in Fig. 3*A*) fails to describe the experimental values, since the thermal stress

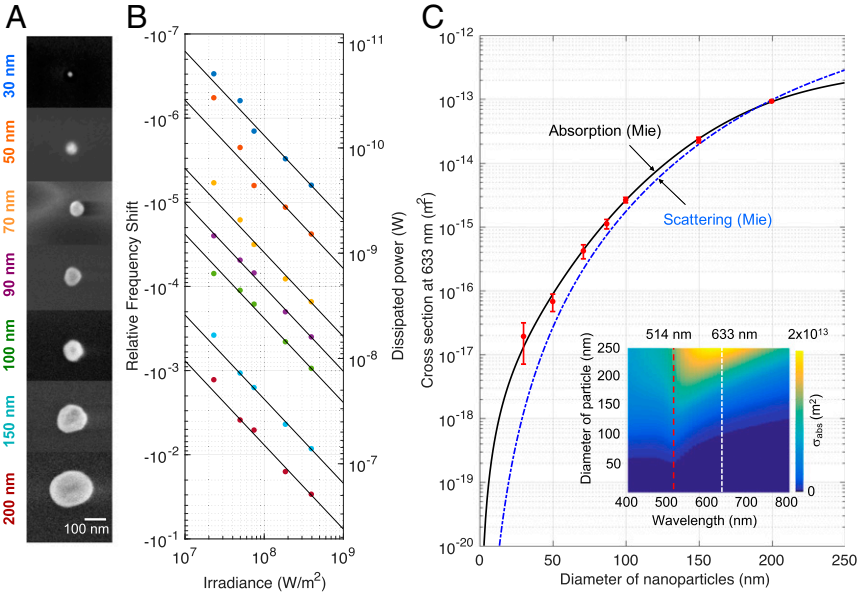

Fig. 2. (*A*) SEM images of AuNPs with different diameter. (*B*) Measured relative frequency shift of silicon nitride drums with 250 MPa of tensile stress for AuNPs with different diameter as a function of irradiance. The dissipated power is calculated from the relative frequency shift via (1). (*C*) Average (>20 particles per size) absorption cross-section as a function of particle size, compared with Mie absorption model and scattering model at 633 nm. (*Inset*) Absorption cross-section spectra for varying AuNP diameter; 514 and 633 nm are marked as red and white dashed lines, respectively.

becomes of the same order of magnitude as the intrinsic tensile stress. Therefore, the full model is plotted (black solid line in Fig. 3*A*), which fits the measured values well.

The minimum detectable absorption cross-section in Fig. 3*A* was calculated with Eq. **2** from the measured responsivities, assuming 100% of thermalization yield, a typical relative frequency stability of $\delta f = 10^{-7}$, and a peak irradiance of $I = 354 \pm 45$ μW/μm^2. From the minimum detectable absorption cross-section, the detection and imaging capability can be classified in two regimes: (*i*) single NP regime with $\sigma_{abs} > 10^{-19}$ m^2 and (*ii*) single molecules with $\sigma_{abs} < 10^{-19}$ m^2. With the current setup, single-NP resolution could be easily achieved even with a stoichiometric silicon nitride drum with 1 GPa of tensile stress. As presented in Fig. 2, drums with 250 MPa of tensile stress allow the detection and analysis of AuNPs down to 30 nm with high reliability. Drums with a tensile stress of 30 MPa are responsive enough to detect and analyze 10-nm AuNPs, as demonstrated in Fig. 1*D*.

To directly show the responsivity enhancement of tensile stress reduction, we plot in Fig. 3*B* scans of 10-nm AuNPs on a drum with different tensile stress but for the same irradiance. Clearly, contrast increases drastically as the initial tensile stress of 30 MPa is reduced to 6 and 1.2 MPa after the oxygen plasma treatments. From the theoretical absorption cross-section of $\sigma_{abs} = 4.2 \times 10^{-19}$ m^2 of a single 10-nm AuNP (based on Mie theory for a wavelength of 633 nm) the corresponding responsivities of $R = \delta f \cdot \sigma_{abs} \cdot I = 50$ kW^{-1} and 311 kW^{-1}, can be calculated for the drums with decreased stress from 30 MPa to 6 and 1.2 MPa, respectively.

After the plasma-induced stress reduction, the obtained responsivities all show the potential for single-molecule imaging, with expected smallest detectable $\sigma_{abs} < 10^{-19}$ m^2, as can be seen from Fig. 3*A*. The limit for stress reduction is given by the required dynamic range, and by background absorption of the probing laser, whose heating-induced stress reduction has to be smaller than the intrinsic tensile stress.

Single-Molecule Detection and Localization

To demonstrate single-molecule sensitivity in a convincing and reliable fashion, a fluorescence dye was chosen due to well-established characteristics, such as single-step photobleaching and blinking, which make the unambiguous identification of single molecules possible. Additionally, a fluorescent dye allows for reference imaging with fluorescence microscopy. Atto 633 was adopted in this study due to the matching of the absorption peak (~630 nm) with our available pump laser wavelength. Atto 633 has an absorption peak at 630 nm and a fluorescence emission peak at 651 nm. For better identification of molecule scans and for reference, we also added highly fluorescent beads during sampling. Fig. 4*A* shows a nanomechanical photothermal scan of three single Atto 633 molecules (numbered as 1, 2, and 3) and one bead (numbered as 4), featuring the highest signal. A reference fluorescence image is provided in Fig. 4*B*. The patterns obtained from both techniques overlap almost perfectly. The actual positions, as shown in the close-up in Fig. 4*E*, were extracted from 2D Gaussian fits and cross-referenced with the fluorescence image to calibrate the pixel size of the absorption image.

To verify that the source of the signal is from single molecules, Atto 633 molecules on the same substrate with similar counts are monitored with fluorescence microscopy, as shown in Fig. 4*B* (*Inset*),and the typical characteristics of single molecules, such as single-step blinking, was observed and demonstrated in Fig. 4*C*. A single Atto 633 molecule is then selected and illuminated with high power, and a single-step photobleaching process is observed, as shown in Fig. 4*D*. In contrast, neither photobleaching nor blinking was observed with our photothermal method under high-vacuum conditions, probably due to the absence of oxygen. However, signals that were bleached under ambient conditions with the fluorescence microscopy setup also disappeared in a subsequent nanomechanical photothermal control scan (*SI Appendix*, Fig. S13). This is evidence for the presence of a single absorber and single emitter, hence a single molecule, in contrast to, e.g., the possibility of the presence of multiple absorbing molecules and one single emitting molecule that got bleached.

Fluorescent molecules dissipate heat either directly via nonradiative relaxation from excited states, or via vibronic relaxation before and after radiative transitions. For Atto 633, the absorption cross-section at 633 nm is calculated from the molar extinction coefficient $\varepsilon_{633} = 1.27 \times 10^5$ M^{-1}·cm^{-1} to be $\sigma_{abs} = 4.84 \times 10^{-20}$ m^2. With the current pumping irradiance of 354 ± 45 μW/μm^2, which is below the measured saturation irradiance of 743 μW/μm^2 of Atto 633 (*SI Appendix*, Fig. S10), this results in a total absorption of 16.7 pW. In Atto 633 only 38.34% of the total absorbed power dissipates into heat through the two nonradiative pathways, which results in a total dissipated power of $P_{abs} = 6.3$ pW. This dissipated power results in a relative frequency detuning of $\delta f = P_{abs} \cdot R = 3.5 \times 10^{-6}$ for a calculated responsivity (based on the nonapproximated model shown as solid black line in Fig. 3*A*) of $R = 558$ kW^{-1} for a silicon nitride drum with $\sigma = 0.8$ MPa with a resonance frequency of $f_0 = 87$ kHz. This gives an absolute frequency detuning of $\Delta f = 0.31 \pm 0.04$ Hz, assuming an optimal polarization alignment between laser and molecules, which fits well with the measured detuning frequencies of $\Delta f =$ 0.25, 0.27, and 0.29 Hz from the single molecules, as presented in the close-up view in Fig. 4*E*. The variance in the measured

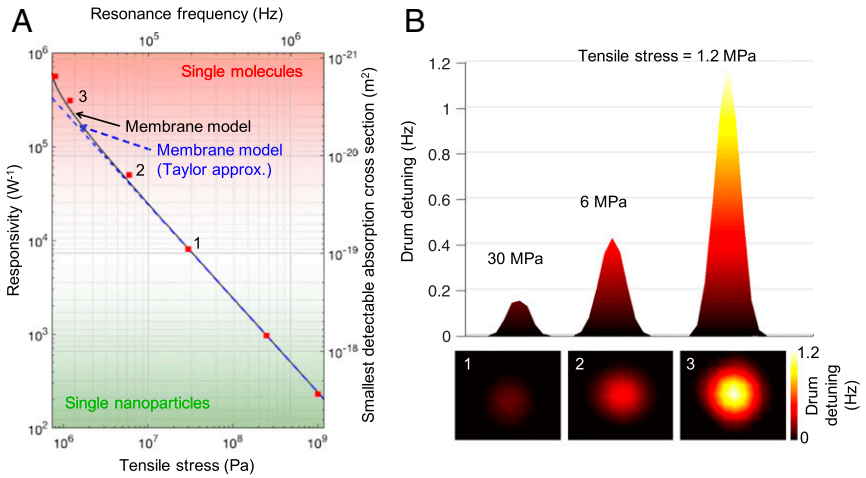

Fig. 3. (*A*) Measured responsivity of silicon nitride drum with different tensile stress (red square). Black solid line is the membrane model and blue dashed line is the Taylor-approximated membrane model. The tensile stress of each drum could be measured by the resonance frequency, and the minimum detectable absorption cross-section at 633 nm could be derived from responsivity and Allan deviation minimum as noise level. (*B*) Drum detuning profile and scans of 10-nm AuNPs with different tensile stress of drum (with initial stress of 30 MPa) after oxygen plasma treatment of 10 and 20 s. The marking numbers correspond to the measurements in *A*.

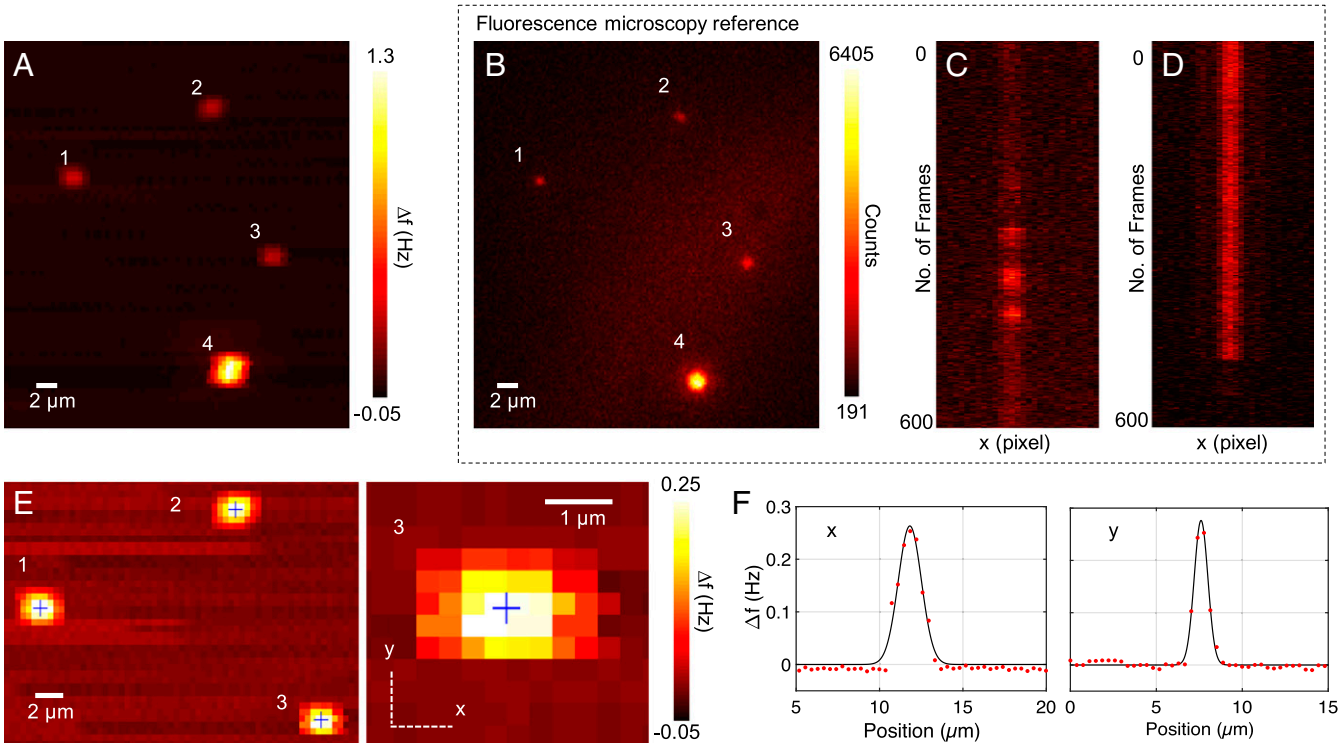

Fig. 4. (*A*) Scan of three single Atto 633 molecules (numbered as 1, 2, and 3) and one fluorescent bead (numbered as 4), measured with the (4,4) mode of a silicon nitride drum with a tensile stress of 0.8 MPa. (*B*) Reference fluorescence microscopy image of *A*. Single molecules on the same substrate were further observed under same conditions for (*C*) blinking and (*D*) bleaching effects. (*E*) Close-up of the three single molecules. The center positions were indicated with the blue crosses. Single molecule no. 3 was further zoomed in. (*F*) Profile cut through the absorption peak of single Atto 633 molecule 3 in *x* and *y* direction, as indicated in *E*.

values can be explained by the individual orientation of the dye molecules, resulting in a varying dipolar excitation by the slightly polarized probing laser (with a polarization of 1:4).

The localization analysis can be used to explore the position accuracy of the measurement and offers a standard comparison with state-of-the-art fluorescent microscopy (*SI Appendix*) (39). With the current long-working-distance 50× objective (N.A. = 0.55), we achieved an average position accuracy of ∼30 nm for single molecules. In comparison, the reference fluorescence measurements for the same sample reached an average position accuracy of ∼15 nm with an oil-immersion 100× objective (N.A. = 1.46). Despite the inferior objective, comparable position accuracies were achieved, which can be attributed to the large signal-to-noise ratio of our method.

From the given responsivity, it is now possible to estimate the sensitivity in terms of absorbed power. For an optimal integration time $\tau = 40$ ms, we measured a typical Allan deviation better than $\Delta f = 4 \times 10^{-3}$ Hz. This gives a relative frequency resolution of $\delta f = \Delta f / f_0 = 4.6 \times 10^{-8}$, resulting in a sensitivity of $S = \delta f \sqrt{\tau} / R = 16$ fW/Hz$^{1/2}$. For a single Atto 633 molecules this gives a signal-to-noise ratio of >70. An absorption profile of a single Atto 633 molecule is presented in Fig. 4*F* in both *x* and *y* directions as indicated in Fig. 4*E*.

Conclusions

In contrast to shot-noise-limited optical probing of sample absorption, nanomechanical probing of the photothermal heating is insensitive to scattering and limited only by thermomechanical noise. The achieved sensitivity at room temperature of 16 fW/Hz$^{1/2}$ is an improvement of five and two orders of magnitude compared with photothermal microscopy (8, 17–21), and shot-noise-limited optical absorption measurements (30, 32), respectively. Compared with state-of-the-art single-molecule imaging techniques, which operate in condensed phase, the required vacuum constitutes an experimental constrain.

The presented mechanical photothermal detection scheme provides an alternative for imaging of nanoobject on nonconducting substrates with improved contrast comparing with SEM. Both the obtained signal-to-noise ratio of >70 for a single molecule and image resolution can further be improved by moving from a 50× to a 100× objective with higher N.A., and with finer scanning steps and decreased pixel spacing. The high signal-to-noise ratio is of particular interest for the precise localization of nonfluorescent single molecules.

The evidence for the imaging of single molecules is based on (*i*) the observation of single bleaching steps of signals and (*ii*) on the measured signal strengths, which agree accurately with the predicted value for single Atto 633 molecules. Polarization-dependent photothermal single-molecule analysis would give the definite proof of the presence of single molecules. Unfortunately, such experiments are not possible with the current setup and will be implemented in the future. While the presented single-molecule evidence is strong and consistent, the missing polarization experiments leave some uncertainty.

Besides the imaging of single nonfluorescent molecules, our technique allows a quantitative absorption analysis of nanoplasmonic structures, such as AuNPs or nanoantennas, with more complexity. For that purpose, the response can be significantly improved by shifting from the 633-nm laser wavelength to around 500 nm, where small AuNPs in particular have an absorption peak maximum.

Furthermore, by using a wavelength tunable scanning laser, e.g., in the infrared regime (37, 40, 41), the presented method can readily be extended to perform hyperspectral absorption microscopy, allowing for the chemical identification, e.g., of single molecules. This is of particular interest for trace analysis in

analytical chemistry application, e.g., as detector for HPLC or capillary electrophoresis.

Methods

Fabrication of Nanomechanical Resonator Substrates. The prestress of the silicon nitride thin film could be defined by the chemical composition of silicon nitride from the low-pressure chemical vapor deposition (LPCVD) process and the subsequent O_2 plasma treatment (38). 50-nm-thick LPCVD stoichiometric silicon nitride with prestress of around 1 GPa and silicon-rich silicon nitride with prestress of around 250 MPa and 30 MPa on Si (100) wafers (Hahn-Schickard Gesellschaft) were used in present experiments. For drums, a simple bulk micromachining process was done from back side, which etched the window with KOH (40 wt %) with etching rate of 50 μm/h (42). Reactive ion etching with O_2 plasma with RF power of 50 W was done on 30 MPa drums for 10 s and 20 s, respectively to further reduce the stress to average of 6 MPa and 1.2 MPa. All drums used in the work had lateral dimension of 530 μm × 530 μm.

Sampling of Analytes. Reactant-free gold NPs with diameters of 10, 20, 30, 50, 80, 90, 100, 150, and 200 nm in 0.1 mM PBS stabilized suspension solution (Sigma-Aldrich) were first diluted in Micropur deionized water (18 MΩ-m; Milli-Q) with ratio of 1:40 at room temperature, respectively, and syringed through polytetrafluoroethylene membrane syringe filters (Acrodisc; Sigma-Aldrich) with a pore size of 200 nm to reduce the aggregations. The filtered solutions were then spin-coated on silicon nitride drums at 2,000 rpm for 10 s and 4,000 rpm for 20 s to evenly distribute the NPs. A volume of 1 μl Atto 633 (BioReagent; Sigma-Aldrich) stock solution (1 mg/mL) was diluted in Micropur deionized water (Milli-Q) with the ratio of 1:1,000 at room temperature, and directly sampled on silicon nitride trampolines with pipette followed by air drying at room temperature for immediate measurements. All sampling processes were also done in cleanroom. The SEM images of NPs were characterized by Hitachi SU8030 with 3-kV acceleration voltage and 20-pA emission current.

Measurement Electronics. The real-time optical readout of a laser Doppler vibrometer (MSA-500; Polytec) after a digital velocity decoder was directly captured by a lock-in amplifier (HF2LI; Zurich Instrument) for the tracking of resonance frequency, as shown in Fig. 1*B*. Five steps of vibrometer 633-nm laser was used with average power of 380, 170, 68.3, 45.5, and 21.2 μW, and focus by 50× objective (0.55 N.A.; Mitutoyo) with nominal FWHM = 0.9 μm and spot size of ∼1.53 μm. In measurements, the averaged FWHM obtained from the measurement is 1.1 ± 0.3918 μm. A piezoelectric element (NAC2003; Noliac) was connected to the output of the lock-in amplifier for actuation. A frequency sweep was performed before every measurement and scanning for the phase locking and to optimize actuation voltage. All experiments were done under high-vacuum condition with chamber pressure below 10^{-4} mbar.

Fluorescence Microscopy. An inverted microscope (Axiovert 200; Zeiss) equipped with a 100×, 1.46 N.A. oil immersion objective (Plan-Apochromat; Zeiss) and a 640-nm diode laser (iBeam smart; Toptica) with a power density of 0.5 kW/cm^2 at the sample was used for imaging. The drum was put upside down on a #1.5 coverslip (24 × 60 mm; Menzel) and up to 1,000 images were recorded with an illumination time of 5 ms and a delay time of 10 ms. All fluorescence measurements were done under ambient condition. Timing protocols were generated and executed with an in-house–written program package implemented in LabVIEW (National Instruments). After appropriate filtering (zt488/640 rpc; Chroma; FF01-538/685–25; Semrock), signals were detected with a back-illuminated EMCCD (electron-multiplying charge-coupled device) camera (iXon Ultra 897; Andor). Experiments were carried out at 22 °C.

ACKNOWLEDGMENTS. We thank Niklas Luhmann and Pedram Sadeghi for their assistance with the measurement and helpful discussions, and Sophia Ewert, Artur Jachimowicz, and Johannes Schalko for their assistance with device fabrication. This work has received funding from the European Research Council under the European Union's Horizon 2020 research and innovation program (Grant Agreement-716087-PLASMECS).

1. Moerner WE, Shechtman Y, Wang Q (2015) Single-molecule spectroscopy and imaging over the decades. *Faraday Discuss* 184:9–36.
2. Sauer M (2013) Localization microscopy coming of age: From concepts to biological impact. *J Cell Sci* 126:3505–3513.
3. Liang F, Guo Y, Hou S, Quan Q (2017) Photonic-plasmonic hybrid single-molecule nanosensor measures the effect of fluorescent labels on DNA-protein dynamics. *Sci Adv* 3:e1602991.
4. Olson J, et al. (2015) Optical characterization of single plasmonic nanoparticles. *Chem Soc Rev* 44:40–57.
5. Zijlstra P, Orrit M (2011) Single metal nanoparticles: Optical detection, spectroscopy and applications. *Rep Prog Phys* 74:106401.
6. Kukura P, et al. (2009) High-speed nanoscopic tracking of the position and orientation of a single virus. *Nat Methods* 6:923–927.
7. Mashaghi A, et al. (2014) Label-free characterization of biomembranes: From structure to dynamics. *Chem Soc Rev* 43:887–900.
8. Cognet L, et al. (2003) Single metallic nanoparticle imaging for protein detection in cells. *Proc Natl Acad Sci USA* 100:11350–11355.
9. Dantham VR, et al. (2013) Label-free detection of single protein using a nanoplasmonic-photonic hybrid microcavity. *Nano Lett* 13:3347–3351.
10. Baaske MD, Foreman MR, Vollmer F (2014) Single-molecule nucleic acid interactions monitored on a label-free microcavity biosensor platform. *Nat Nanotechnol* 9:933–939.
11. Vollmer F, Arnold S, Keng D (2008) Single virus detection from the reactive shift of a whispering-gallery mode. *Proc Natl Acad Sci USA* 105:20701–20704.
12. Zijlstra P, Paulo PMR, Orrit M (2012) Optical detection of single non-absorbing molecules using the surface plasmon resonance of a gold nanorod. *Nat Nanotechnol* 7:379–382.
13. Li B-B, et al. (2014) Single nanoparticle detection using split-mode microcavity Raman lasers. *Proc Natl Acad Sci USA* 111:14657–14662.
14. Zhu J, et al. (2010) On-chip single nanoparticle detection and sizing by mode splitting in an ultrahigh-Q microresonator. *Nat Photonics* 4:46–49, and erratum (2010) 4:122.
15. Bohren CF, Huffman DR (1998) *Absorption and Scattering of Light by Small Particles* (Wiley-VCH Verlag GmbH, Weinheim, Germany), p 544.
16. Moerner WE, Kador L (1989) Optical detection and spectroscopy of single molecules in a solid. *Phys Rev Lett* 62:2535–2538.
17. Boyer D, Tamarat P, Maali A, Lounis B, Orrit M (2002) Photothermal imaging of nanometer-sized metal particles among scatterers. *Science* 297:1160–1163.
18. Gaiduk A, Yorulmaz M, Ruijgrok PV, Orrit M (2010) Room-temperature detection of a single molecule's absorption by photothermal contrast. *Science* 330:353–356.
19. Gaiduk A, Ruijgrok PV, Yorulmaz M, Orrit M (2010) Detection limits in photothermal microscopy. *Chem Sci* 1:343–350.
20. Berciaud S, Cognet L, Blab GA, Lounis B (2004) Photothermal heterodyne imaging of individual nonfluorescent nanoclusters and nanocrystals. *Phys Rev Lett* 93:257402.
21. Cognet L, Berciaud S, Lasne D, Lounis B (2008) Photothermal methods for single nonluminescent nano-objects. *Anal Chem* 80:2288–2294.
22. Nedosekin DA, Galanzha EI, Dervishi E, Biris AS, Zharov VP (2014) Super-resolution nonlinear photothermal microscopy. *Small* 10:135–142.
23. Ding TX, Hou L, Meer Hv, Alivisatos AP, Orrit M (2016) Hundreds-fold sensitivity enhancement of photothermal microscopy in near-critical Xenon. *J Phys Chem Lett* 7:2524–2529.
24. Chang WS, Link S (2012) Enhancing the sensitivity of single-particle photothermal imaging with thermotropic liquid crystals. *J Phys Chem Lett* 3:1393–1399.
25. Kim J-W, Galanzha EI, Shashkov EV, Moon H-M, Zharov VP (2009) Golden carbon nanotubes as multimodal photoacoustic and photothermal high-contrast molecular agents. *Nat Nanotechnol* 4:688–694.
26. Hong X, et al. (2011) Background-free detection of single 5 nm nanoparticles through interferometric cross-polarization microscopy. *Nano Lett* 11:541–547.
27. Lindfors K, Kalkbrenner T, Stoller P, Sandoghdar V (2004) Detection and spectroscopy of gold nanoparticles using supercontinuum white light confocal microscopy. *Phys Rev Lett* 93:037401.
28. Arbouet A, et al. (2004) Direct measurement of the single-metal-cluster optical absorption. *Phys Rev Lett* 93:127401.
29. Kukura P, Celebrano M, Renn A, Sandoghdar V (2010) Single-molecule sensitivity in optical absorption at room temperature. *J Phys Chem Lett* 1:3323–3327.
30. Celebrano M, Kukura P, Renn A, Sandoghdar V (2011) Single-molecule imaging by optical absorption. *Nat Photonics* 5:95–98.
31. Lo SS, Devadas MS, Major TA, Hartland GV (2013) Optical detection of single nano-objects by transient absorption microscopy. *Analyst* 138:25–31.
32. Chong S, Min W, Xie XS (2010) Ground-state depletion microscopy: Detection sensitivity of single-molecule optical absorption at room temperature. *J Phys Chem Lett* 1:3316–3322.
33. Heylman KD, et al. (2016) Optical microresonators as single-particle absorption spectrometers. *Nat Photonics* 10:788–795.
34. Schmid S, Wu K, Larsen PE, Rindzevicius T, Boisen A (2014) Low-power photothermal probing of single plasmonic nanostructures with nanomechanical string resonators. *Nano Lett* 14:2318–2321.
35. Larsen T, Schmid S, Villanueva LG, Boisen A (2013) Photothermal analysis of individual nanoparticulate samples using micromechanical resonators. *ACS Nano* 7:6188–6193.
36. Wu H, Grabarnik S, Emadi A, De Graaf G, Wolffenbuttel RF (2009) Characterization of thermal cross-talk in a MEMS-based thermopile detector array. *J Micromech Microeng* 19:074022.
37. Kurek M, et al. (2017) Nanomechanical infrared spectroscopy with vibrating filters for pharmaceutical analysis. *Angew Chem Int Ed Engl* 56:3901–3905.
38. Luhmann N, et al. (2017) Effect of oxygen plasma on nanomechanical silicon nitride resonators. *Appl Phys Lett* 111:63103.
39. Mortensen KI, Churchman LS, Spudich JA, Flyvbjerg H (2010) Optimized localization analysis for single-molecule tracking and super-resolution microscopy. *Nat Methods* 7:377–381.
40. Andersen AJ, et al. (2016) Nanomechanical IR spectroscopy for fast analysis of liquid-dispersed engineered nanomaterials. *Sens Actuators B* 233:667–673.
41. Yamada S, Schmid S, Larsen T, Hansen O, Boisen A (2013) Photothermal infrared spectroscopy of airborne samples with mechanical string resonators. *Anal Chem* 85:10531–10535.
42. Williams KR, Member S, Gupta K, Member S, Wasilik M (2003) Etch rates for micromachining processing—Part II. *J Microelectromech Syst* 12:761–778.